Single-walled carbon nanotubes as a multimodal-thermoacoustic and photoacoustic-contrast agent

Manojit Pramanik
Washington University in St. Louis
Department of Biomedical Engineering
Optical Imaging Laboratory
Campus Box 1097
1 Brookings Drive
St. Louis, Missouri 63130
E-mail: mano@biomed.wustl.edu

Magdalena Swierczewska
Danielle Green
Balaji Sitharaman
Stony Brook University
348 Psychology A Building Biomedical Engineering
Stony Brook, New York 11794

Lihong V. Wang
Washington University in St. Louis
Department of Biomedical Engineering
Optical Imaging Laboratory
Campus Box 1097
1 Brookings Drive
St. Louis, Missouri 63130

Abstract. We have developed a novel carbon nanotube-based contrast agent for both thermoacoustic and photoacoustic tomography. In comparison to deionized water, single-walled carbon nanotubes exhibited more than twofold signal enhancement for thermoacoustic tomography at 3 GHz. In comparison to blood, they exhibited more than sixfold signal enhancement for photoacoustic tomography at 1064 nm wavelength. The large contrast enhancement of single-walled carbon nanotubes was further corroborated by tissue phantom imaging studies. © *2009 Society of Photo-Optical Instrumentation Engineers.* [DOI: 10.1117/1.3147407]

Keywords: thermoacoustic tomography; photoacoustic tomography; contrast agents; single-walled carbon nanotubes; carbon nanotubes.

Paper 09048R received Feb. 13, 2009; revised manuscript received Mar. 22, 2009; accepted for publication Mar. 26, 2009; published online Jun. 8, 2009.

1 Introduction

The advent of numerous noninvasive imaging modalities, such as X-ray, computed tomography, single photonemission-computed tomography, positron emission tomography (PET), magnetic resonance imaging (MRI), ultrasound imaging, radio frequency (rf), and optical imaging now allows scientists and clinicians to acquire *in vivo* images of the anatomy and physiology of animals and humans.[1,2] Each of these *in vivo* imaging techniques possesses characteristic strengths and weaknesses. For each imaging modality, substantial attention has been devoted to developing contrast agents not only for improving the contrast of the acquired images, but also for molecular imaging targeting specific biomolecules, cell tracking, and gene expression.[3–6]

We have developed hybrid imaging modalities, such as thermoacoustic (TA) tomography (TAT) and photoacoustic (PA) tomography (PAT), for different applications[7–11] and combined these two imaging modalities into a single imaging system for early breast cancer detection.[12] Diagnosis of cancer in its early stages depends on the recognition of subtle changes in tissue properties, such as mechanical properties, optical absorption, and rf absorption. For example, changes in ion and water concentrations lead to changes in rf absorption. To detect these changes, nonionizing rf electromagnetic waves and visible/near infrared (NIR) light-based imaging modalities have generated particular interest over the last decade.[7–11,13–17] TAT/PAT synergizes the advantages of pure-ultrasound and pure-rf/optical imaging,[7,13] allowing both satisfactory spatial resolution and high soft-tissue contrast. For instance, PAT is a unique noninvasive technology for imaging and quantifying the levels of vascularization and oxygen saturation in tumors.[9–11,18,19] These features are associated with angiogenesis and hypoxia accompanying malignant tumors.[20,21] TAT/PAT is also capable of revealing information such as water/ion concentration, blood volume, and oxygenation of hemoglobin. Because these parameters can change during the early stages of cancer, TAT/PAT offers opportunities for early detection. However, even though high rf and optical contrast exists between well-developed malignant tumor tissue and normal human breast tissue, the contrast during very early stages of cancer may be insufficient. Thus, a targeted contrast agent could be greatly beneficial for early cancer diagnosis using TAT/PAT.

Recently, carbon nanotube-based contrast agents have shown promise for a variety of imaging techniques.[22–25] The strategies for development of these contrast agents have included encapsulation of medically relevant metal ions within their carbon sheath,[22] external functionalization of the carbon sheath with a variety of imaging agents,[23,24] and exploiting the intrinsic physical properties of the carbon nanotubes.[25] In this work, we have explored the intrinsic optical[26,27] and rf[28] absorbing properties of single-walled carbon nanotubes (SWNTs) with the goal of developing them as multimodal

Address all correspondence to: Balaji Sitharaman, Department of Biomedical Engineering, State University of New York at Stony Brook, Stony Brook, NY 11794; Tel: 631-632-1810; E-mail: balaji.sitharaman@stonybrook.edu; and Lihong V. Wang, Optical Imaging Laboratory, Department of Biomedical Engineering, Washington University in St. Louis, Campus Box 1097, One Brookings Drive, St. Louis, MO 63130; Tel: 314-935-6152; Fax: 314-935-7448; E-mail: lhwang@biomed.wustl.edu

1083-3668/2009/14(3)/034018/8/$25.00 © 2009 SPIE

contrast agents for simultaneous TAT and PAT.

2 Methods and Materials

2.1 *TAT/PAT Scanner*

A combined TAT/PAT scanner[12] was used for all the experimental studies in this work. Images were collected with microwave excitation (TAT) and then with laser excitation (PAT). For TAT, a 3.0-GHz microwave source with a 0.5-μs pulse width and 100-Hz pulse repetition rate was the rf source. The pulse energy was estimated to be around $\sim$10 mJ ($=20\ \text{kW}\times 0.5\ \mu\text{s}$), falling within the IEEE safety standards.[29] PAT was done at 1064 nm wavelength. A Q-switched Nd:YAG laser with a 10-Hz pulse repetition rate, 6.5-ns (at 1064 nm wavelength) laser pulse width, and 850-mJ maximal output energy was the light source. The incident laser fluence on the sample surface was controlled to be $<20\ \text{mJ/cm}^2$, conforming to the American National Standards Institute (ANSI) standards.[30] The generated acoustic signals were detected using two different nonfocused transducers operating at a 2.25-MHz central frequency (13-mm-diam active area, ISS 2.25×0.5 COM; 6-mm-diam active area, ISS 2.25×0.25 COM, Krautkramer). For cross-sectional TAT/PAT imaging, data were collected around the sample in a full circle. Different reconstruction algorithms can be used to reconstruct TAT/PAT images from raw data.[16] Here, a delay and sum (backprojection) algorithm was used for all image reconstruction.[16] The sample was placed inside the breast holder chamber, which was filled with mineral oil. Mineral oil does not absorb microwaves. Moreover, because mineral oil is transparent, the light absorption is also very small. Mineral oil also acts as a coupling medium for sound propagation. Thus for all our experiments, mineral oil was an ideal choice as a background medium.

2.2 *PA Imaging System*

A reflection-mode PA imaging system[31] was used to test the *in vitro* blood signal enhancement using the SWNTs. A tunable Ti:sapphire laser (LT-2211A, LOTIS TII) pumped by a Q-switched Nd:YAG (LS-2137, LOTIS II) laser was the light source, providing $<$15-ns pulse duration and a 10-Hz pulse repetition rate. A 5-MHz central frequency, spherically focused ultrasonic transducer (V308, Panametrics-NDT) was used to acquire the generated PA signals. The transducer had a 2.54-cm focus length, a 1.91-cm-diam active area element, and 72% bandwidth. The signal was then amplified by a low-noise amplifier (5072PR, Panametrics-NDT), and recorded using a digital oscilloscope (TDS 5054, Tektronix) with a 50 mega-sampling rate. PA signal fluctuations due to pulse-to-pulse energy variation were compensated by signals from a photodiode (DET110, Thorlabs), which sampled the energy of each laser pulse.

2.3 *SWNTs Synthesis*

A diblock copolymer templating method was used to coat Fe coated on Si wafers.[32] The wafers were placed in a 3-in. quartz reaction chamber (Easy Tube 2000, First Nano) and heated in Ar to 900 °C. The chamber was filled with H_2 for 2 min, and CH_4 was added to the gas flow as the carbon feedstock for 20 min to initiate the growth of SWNTs. Subsequently, the carbon feedstock was switched off and the furnace was cooled to room temperature. Raman spectroscopy (LabRAM Aramis, Horiba JvonYvon) at 633-nm excitation, transmission electron microscope (TEM) imaging (JEOL 2000 FX electron microscope operating at 200 kV), ζ potential (Malvern Zetasizer NanoZS system with irradiation from a 632.8-nm He–Ne laser), and atomic force microscopy [(AFM) MFD-3D-BIO, Asylum Research] were used to characterize the SWNTs.

Figure 1(a) shows a representative bright-field TEM image of densely populated SWNTs on the surface of the substrate. Further investigation by high-resolution TEM (HRTEM) [Fig. 1(b)] and AFM [Fig. 1(c)] showed SWNTs with diameters between 1.2 and 2.2 nm and lengths between 500 nm and 1 μm. Figure 1(d) shows a representative Raman spectrum of SWNTs at the laser excitation wavelength of 633 nm. The Raman spectrum shows a G band at 1596 cm^{-1} and a D band at 1320 cm^{-1}, with a D/G band ratio for Gd-SWNTs of <0.1, indicating that the SWNTs have very few defects.[33] The radial breathing modes [Fig. 1(d) inset], unique to SWNTs,[33] further corroborate the HRTEM and AFM results and confirm the presence of SWNTs. Four types of multiwalled carbon nanotubes (MWNTs) of various inner and outer diameters, fullerenes (Sigma-Aldrich, USA, catalog number 483036), and graphite microparticles (Sigma-Aldrich, catalog number 496596) were also used for initial studies. SWNT suspensions with different concentrations (0.1–1 mg/mL) were prepared in 10 mL of 1% biologically compatible Pluronic® F127 surfactant solution (pH 7). The different domains of the nonionic Pluronic F127 likely wrapped themselves in energy-minimized conformations around the nanotubes to solubilize the SWNTs by steric stabilization, producing nearly neutral nanotube suspensions.[34] These suspensions were stable during the period of the entire study. The ζ-potential measurements were performed on 0.1 mg/mL SWNTs dispersed in Pluronic F-127 and showed a peak ζ potential of -14 mV with a Gaussian distribution (full width half maximum of the distribution$=10$ mV). This value is similar to other reported ζ-potential measurements on neutral stable SWNTs dispersed in Pluronic F127.[34] Figure 1(e) shows an optical image of the SWNTs (0.1–1 mg/mL concentration) dispersed in Pluronic F127 after aggressive sonication.

3 Results and Discussions

A low-density polyethylene (LDPE) vial with an inner diameter of 6 mm and 1 cc volume was used as a sample holder for the entire study. The vial was filled with the sample and placed inside the TAT/PAT scanner. Deionized (DI) water was used for TA signal comparison, whereas blood was used for PA signal comparison. Water and ions are two well-known sources of microwave absorbers in the human body, and they produce strong TA signals. Therefore, to show that a new material (in this case, SWNTs) can function as a contrast agent, we have to first show that SWNTs are capable of generating TA signals comparable to or stronger than a known TA signal producer in the body. The rf contrast between malignant tumor tissue and normal human breast tissue is as high as 4:1.[35] The rf absorption of water compared to background human breast tissue is also on the order of 4:1. Thus, we compared the rf absorption of SWNTs to that of water. Simi-

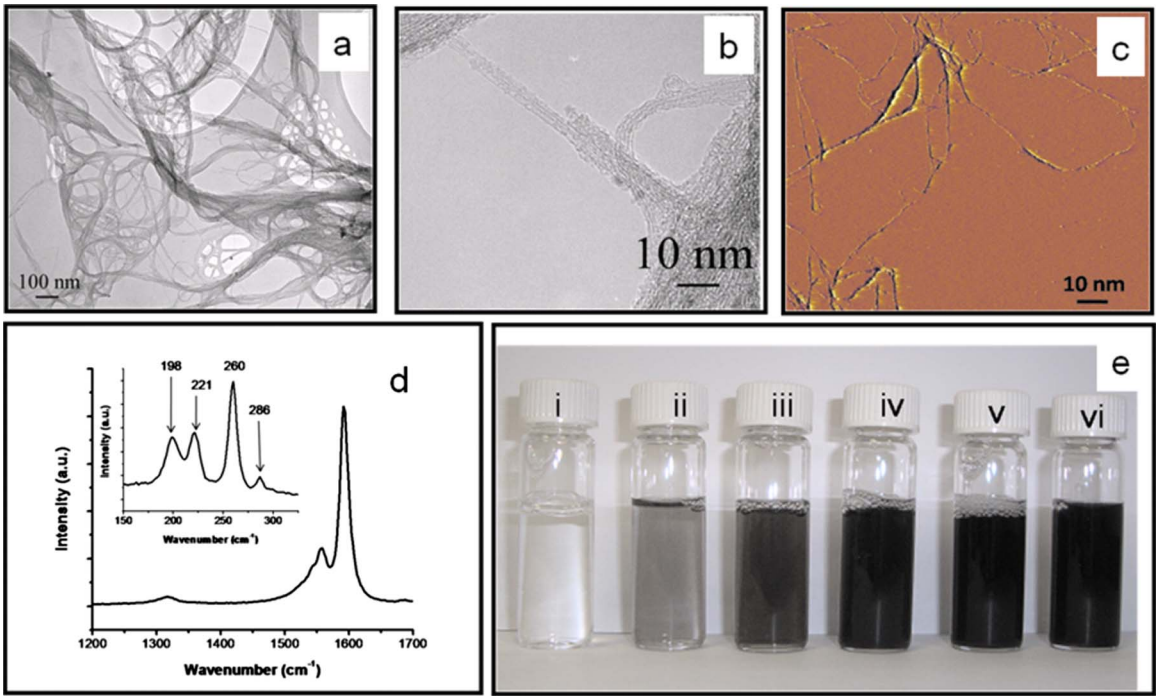

Fig. 1 (a) A low-resolution bright-field TEM, (b) HRTEM image of bundled SWNTs grown using Fe as the catalyst. (c) Tapping mode AFM images of dispersed SWNTs. (d) D-band and G-band Raman spectra of the SWNTs. The inset shows the radial breathing modes. (e) Vials contain aqueous dispersions of SWNTs in Pluronic F127 after being sonicated. From left to right, the concentrations are (i) 0, (ii) 0.1, (iii) 0.25, (iv) 0.5, (v) 0.75, and, (vi) 1 mg/mL. (Color online only.)

larly, blood is a dominant light absorber in the human body and produces strong PA signals. Therefore, to show that SWNTs can function as a contrast agent in PA, we must first show that SWNTs are capable of generating PA signals comparable to or stronger than that of a known absorber in the body. Blood was thus an obvious choice for comparison here. For the tissue phantom imaging, porcine fat was used as the background medium mimicking the tissue; the sample holder (LDPE vial) was inserted in the center of a ~6-cm-diam porcine fat cylinder of ~1.5 cm high. The vial was filled with different samples (DI water, SWNTs, and blood) and images were collected. The hole inside the porcine fat had a slightly larger diameter than the sample holder's outside diameter.

Figure 2(a) shows the TA signal generated from the sample holder (LDPE vial) filled with DI water and with mineral oil. As we can clearly see, there is no TA signal from the sample holder filled with mineral oil (red line, showing only the noise of the system, no TA signal was observed). Therefore, the LDPE vial does not generate any TA signal. Moreover, the LDPE vial we used is semi-transparent white and, therefore, it does not absorb enough light to produce any measurable PA signal. Nevertheless, we tested the LDPE vial filled with blood and mineral oil under 1064-nm wavelength light. Figure 2(b) shows the PA signal generated from the vial. It is clearly seen that vial filled with mineral oil does not produce any significant PA signal at 1064 nm compared to the signal generated from blood. Therefore, we conclude that the sample holder vial has no effect either in TA or in PA signal generation, and henceforth, all signals observed are considered to be generated from the sample placed inside the vial. We also tested the 1% Pluronic F127 surfactant solution and observed no significant TA/PA signals. Figure 2(c) shows the TA signal generated from the LDPE vial filled with 1% Pluronic F127 surfactant solution and DI water, and there is no significant contribution from the surfactant solution. Figure 2(d) shows the PA signal generated from blood and 1% Pluronic F127 surfactant solution. Clearly, there is no PA signal generated from 1% Pluronic F127 surfactant solution. Therefore, any

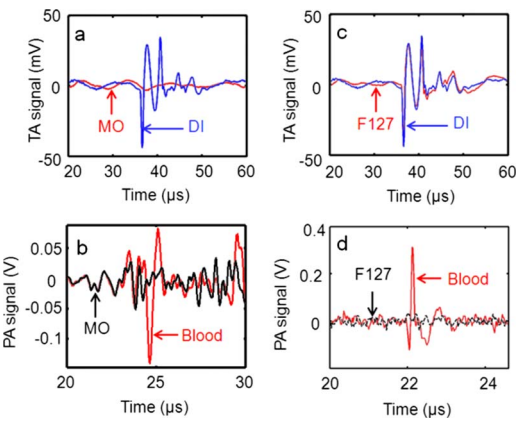

Fig. 2 (a) TA signals from a LDPE vial (i.d. 6 mm, volume 1 cc) filled with mineral oil (MO) and DI water (DI). (b) PA signals from LDPE vial filled with blood and MO at 1064 nm. (c) TA signals from the LDPE vial filled with 1% Pluronic F127 solution (F127) and Deionized water (DI). (d) PA signals from a tube (Silastic® laboratory tubing, Dow Corning Corp., with 300 μm i.d., 640 μm o.d.) filled with blood and with 1% Pluronic F127 solution (F127). (Color online only.)

Table 1 Peak-to-peak TA/PA signal amplitudes obtained from various samples. A LDPE (6 mm i.d., 1 cc volume) vial was the sample holder. TA was done at 3 GHz, and PA was done at 1064 nm wavelength.

	Peak-to-peak TA signal amplitude (mV)		Peak-to-peak PA signal amplitude (mV)	
Sample	0.5-in. active area transducer	0.25-in. active area transducer	0.5-in. active area transducer	0.25-in. active area transducer
Deionized water	47	14	—	—
SWNT (1 mg/mL)	95	28	113	81
Fullerene (C_{60})	51	15	55	68
Graphite microparticles	38	10	28	30
MWNT (o.d.=10–15 nm)	40	12	95	81
Aldrich MW NT (o.d.=20–30 nm)	40	12	58	67
MWNT (o.d.=40–70 nm)	39	10	28	27
MWNT (o.d.=110–170 nm)	47	15	62	70
Blood	—	—	33	31

TA/PA signal contribution coming from the Pluronic F127 will be ignored in all future discussion.

An initial assessment was made for all the carbon nanostructures (SWNTs, MWNTs, C_{60}, and graphite microparticles). Table 1 summarizes the peak-to-peak TA/PA signal amplitudes obtained from various samples with the two different diameter transducers. Among all the samples, only SWNTs showed a significant increase in TA signal compared to DI water and a significant increase in PA signal compared to rat blood. To avoid overinterpretation of the data presented in Table 1, it is important to mention here that the TA and PA signals generated from the MWNT are not directly proportional to the outer diameter. Other parameters, such as the inner diameter, nanotube length, and number of concentric nanotubes, may also affect the generated signal amplitudes. The only conclusion that can be drawn from Table 1 is that the SWNT sample generates a PA and TA signal stronger than that from blood, water, and other carbon nanostructures. The increases in TA and PA signals were shown by pristine SWNTs (mass of Fe is ~20% of total weight of the SWNT sample) as well as purified SWNTs (mass of Fe is ~0.5–1% of the total weight of the SWNT sample), clearly indicating that the observed effects were due to the SWNTs and not due to the presence of iron. Because only SWNTs showed a significant increase in both TA and PA signals, they were used for further studies.

Figure 3(a) displays the TA signals from an LDPE vial filled with DI water and another vial filled with 1-mg/mL SWNTs. The peak-to-peak TA signal amplitudes generated by DI water and 1-mg/mL SWNTs are 42 ± 0.32 and 101 ± 0.24 mV, respectively. Figure 3(b) shows the peak-to-peak TA signal amplitude and fractional increase in TA signal versus the concentration of SWNTs. The largest standard deviation of the data points, measuring 0.92 mV, was observed at 0.75-mg/mL concentration SWNTs. The data show an approximately linear relationship between the TA signal amplitude and the SWNTs' concentration. We observe a maximum of 140% increase in the peak-to-peak signal amplitude for 1 mg/mL SWNTs over DI water. Figure 3(c) displays the PA signals from LDPE vial filled with blood and with 1 mg/mL SWNTs. The peak-to-peak PA signal amplitudes generated by blood, and the 1-mg/mL SWNTs are 0.22 ± 0.002 and 1.32 ± 0.009 V, respectively. Figure 3(d) shows the peak-to-peak PA signal amplitude and fractional increase in PA signal versus the concentration of SWNTs. The largest standard deviation of the data points, measuring 0.027 V, was again observed at 0.75-mg/mL concentration SWNTs. The data again show an approximately linear relationship between the PA signal amplitude and the SWNTs' concentration. We observe a maximum 490% increase in the peak-to-peak signal for 1-mg/mL SWNTs over blood. *In vitro* tests were carried out with SWNTs (0.1 mg/mL) mixed with blood in different proportions, and then PA signals were recorded. Keeping in mind that in other applications NIR light (700–800 nm) would be used for *in vivo* deep tissue imaging, the light used here was of 754 nm wavelength in the reflection mode PA imaging system.[31] A tube (Silastic® laboratory tubing, Dow Corning Corp., with 300 μm, i.d. 640 μm o.d.) was filled with blood, blood (90% v/v)+SWNTs (10% v/v), blood (75% v/v)

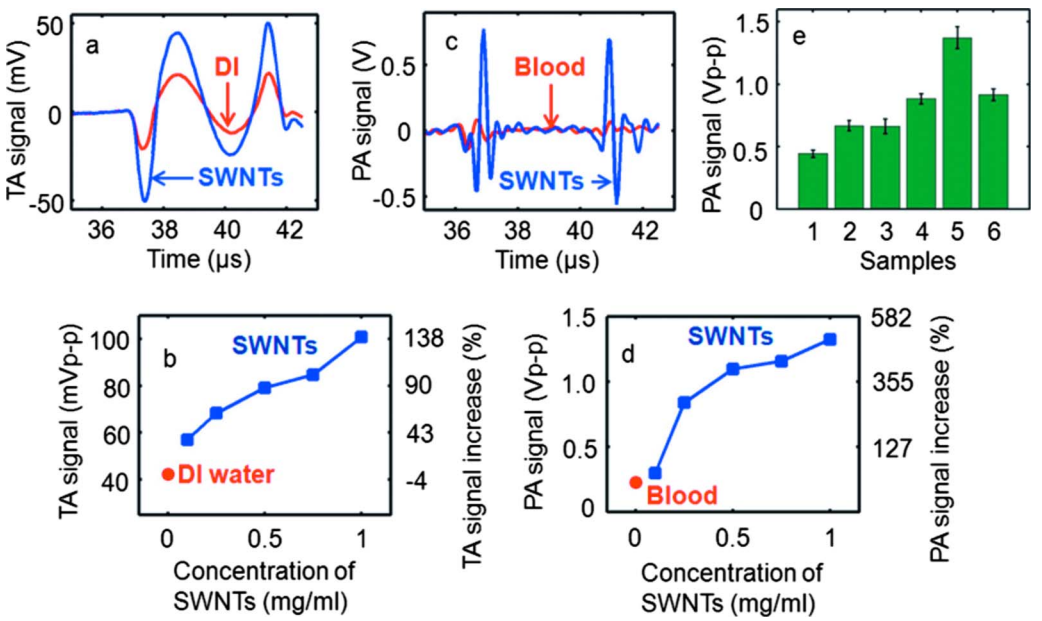

Fig. 3 (a) TA signals at 3 GHz from a LDPE vial (i.d. 6 mm, volume 1 cc) filled with DI water and 1-mg/mL SWNTs. (b) Peak-to-peak TA signal amplitude and fractional increase in TA signal versus SWNTs concentration. (c) PA signals at 1064 nm wavelength from a LDPE vial filled with rat blood and 1-mg/mL SWNTs. (d) Peak-to-peak PA signal amplitude and fractional increase in PA signal versus SWNTs concentration. (e) Peak-to-peak PA signal amplitudes from blood mixed with various amounts of SWNTs. 1: Blood only, 2: blood (90% v/v)+SWNTs (10% v/v), 3: blood (75% v/v)+SWNTs (25% v/v), 4: blood (50% v/v)+SWNTs (50% v/v), 5: blood (25% v/v)+SWNTs (75% v/v), and 6: SWNTs alone. The light source was of 754 nm wavelength. A tube (Silastic laboratory tubing, Dow Corning Corp., with 300 μm i.d., 640 μm o.d.) was used to hold the sample. (Color online only.)

+SWNTs (25% v/v), blood (50% v/v)+SWNTs (50% v/v), blood (25% v/v)+SWNTs (75% v/v), and SWNTs alone. Figure 3(e) shows the peak-to-peak PA signal amplitudes for those six samples, clearly indicating that the PA signal from blood was enhanced when SWNTs were mixed with the blood. The experiments were carried out 10 times to get the average and the standard deviation. We observed a PA signal of 1.37 ± 0.09 V from a mixture of 75% SWNTs and 25% blood, compared to a 0.44 ± 0.02 V PA signal from only blood. Therefore, when SWNTs were mixed with the blood, we saw a >210% increase in the PA signal at 754 nm wavelength.

Next, LDPE vials filled with different SWNTs samples were imaged in two dimensions using TAT and PAT. Figures 4(a) and 4(b) show the TAT cross-sectional image of a vial filled with DI water and SWNTs, respectively, clearly demonstrating a substantial improvement in the TA signal for the vial filled with SWNTs (both figures are shown in the same range of the color bar). Figures 4(c) and 4(d) compare the image profiles along the horizontal and vertical lines [dotted lines in Figs. 4(a) and 4(b)], respectively. Compared to DI water, SWNTs showed ~1.9 times and ~2.1 times signal improvements in the TA image along the horizontal and vertical lines, respectively (normalized to DI water). These results are consistent with the TA data presented in Fig. 3. Figures 4(e) and 4(f) show cross-sectional PAT images of the vial filled with blood and SWNTs, respectively, showing an increased signal in the PAT images with SWNTs compared to blood (both figures are shown in the same range of the color bar). Figures 4(g) and 4(h) compare the image profiles along the horizontal and vertical lines [along the dotted lines in Figs. 4(e) and 4(f)], respectively. Compared to blood, SWNTs showed a ~6.3-fold signal improvement along the horizontal line and ~5.6-fold signal improvement along the vertical line (normalized to blood). These results are consistent with the PA data presented in Fig. 3. The variation in the signal improvement along the horizontal and vertical directions for both TAT and PAT is possibly due to the anisotropic spatial resolution.

Figures 4(i) and 4(j) show the reconstructed tissue-mimicking phantom TAT images for DI water and SWNTs, respectively. The dark spot on the image, marked with a solid arrow, is a needle used to hold the tissue sample. The boundary of the fat tissue is marked with a dashed arrow. The images clearly show greater contrast for the SWNTs-filled vial than for the DI-water-filled vial. Figures 4(k) and 4(l) show PAT images with blood and SWNTs, respectively, for the tissue phantom. The results are similar to those obtained by TAT imaging: the SWNT sample displays greater contrast than blood.

The main motivation in this study was to show that SWNTs can themselves generate both TA and PA signals. Toward this end, as discussed above, a nonionic, nearly neutral SWNT solution was used for the phantom imaging because, in the future, *in vivo* imaging studies will be carried out by injecting SWNTs in solution (most probably in a buffer solution with water as its main component) instead of solid SWNT powder. Our results show that SWNTs could be used for TA/PA imaging, because the intrinsic absorption properties of SWNTs are able to produce equivalent or stronger (depending on the SWNTs concentrations) TA/PA signals than a known endogenous absorber (more than water in the case of TAT and more than blood in the case of PAT). Additionally, a

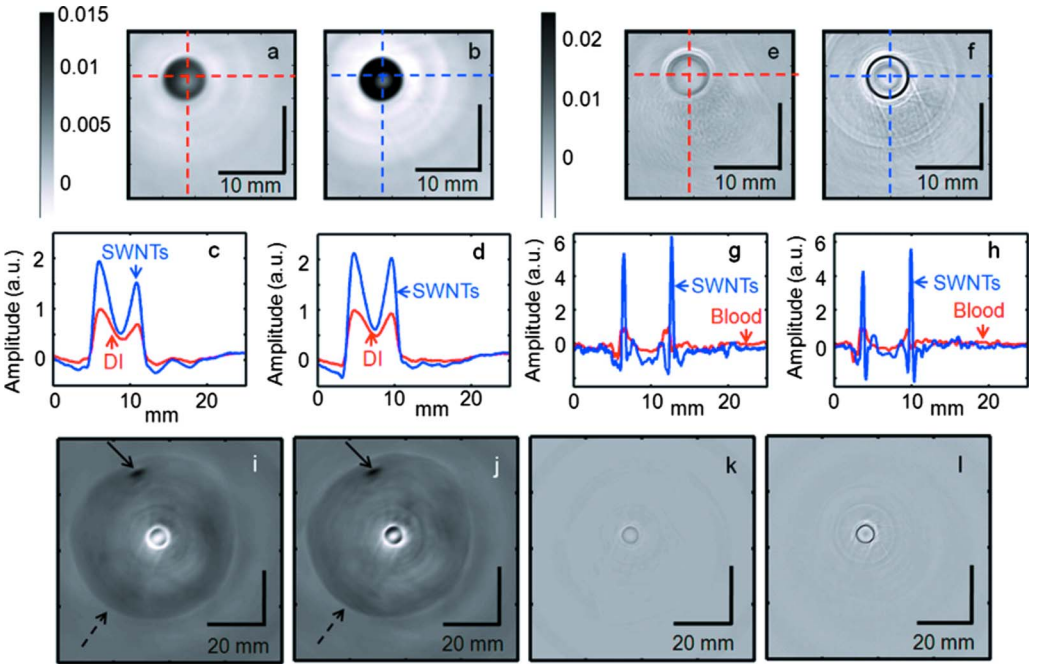

Fig. 4 (a) Cross-sectional TAT image of the vial (LDPE, 6 mm i.d., 1 cc volume) containing DI water. (b) Cross-sectional TAT image of the vial containing 1-mg/mL SWNTs. (c) Comparison of the signal profiles along the horizontal lines across the centers of the vials in (a) and (b). (d) Comparison of the signal profiles along the vertical lines across the centers of the vials in (a) and (b). (e) Cross-sectional PAT image of the vial containing blood. (f) Cross-sectional PAT image of the vial containing 1-mg/mL SWNTs. (g) Comparison of the signal profiles along the horizontal lines across the centers of the vials in (e) and (f). (h) Comparison of the signal profiles along the vertical lines across the centers of the vials in (e) and (f). (i) Cross-sectional TAT image of the vial containing DI water inside pork fat tissue. (j) Cross-sectional TAT image of the vial containing 1-mg/mL SWNTs inside pork fat tissue. The solid arrow points to the needle used to hold the fat tissue, and the dashed arrow indicates the boundary of the fat tissue. (k) Cross-sectional PAT image of the blood vial inside pork fat tissue. (l) Cross-sectional PAT image of the 1-mg/mL SWNTs vial inside pork fat tissue. (Color online only.)

substantial enhancement in the PA signal was measured *in vitro* when the SWNTs were mixed with blood. Thus, we conclude that when the SWNT solution is mixed with water/blood, it enhances the total TA/PA signal from the water/blood. Furthermore, TA/PA signals generated by SWNTs could be used for imaging applications where there are no endogenous signals. For example, using PA imaging and SWNTs, we have carried out *in vivo* sentinel lymph-node mapping noninvasively.[36] In this application, there was no blood signal involved and the PA signals generated by the SWNTs were used for imaging the sentinel lymph nodes. Another example is a targeted molecular imaging application, where the TA/PA signal would be generated from the contrast agents themselves.

As shown in previous studies,[37] the optical absorption properties of SWNTs are strong in the visible and NIR region. Currently, no studies have demonstrated SWNTs' absorption property in the 3-GHz microwave region, but their conductive properties make them promising for strong absorption.[38] SWNTs have high permittivity when exposed to electromagnetic radiation at frequencies between 0.5 and 3 GHz, and as the frequency increases to >3 GHz, the permittivity decreases,[39,40] indicating that SWNTs could be used as contrast agents at <3 GHz. Another study showed the feasibility of iron oxide nanoparticles as a contrast agent in TAT.[41] To the best of our knowledge, this is the first study that explores the efficacy of SWNTs as contrast agents for multimodal imaging with TAT/PAT. This study successfully demonstrates that SWNTs are suitable as a contrast agent for both TAT and PAT. The SWNTs also allow contrast-enhanced deep-tissue imaging with TAT. In this study, for TAT, we observed contrast enhancement due to the SWNTs at an rf frequency of 3 GHz. It will be particularly interesting to characterize their effectiveness at lower rf frequencies. It is well known that the human body becomes more transparent at lower rf frequencies, allowing an increase in the imaging depth. However, because of lower tissue absorbance at lower rf frequencies, the intrinsic image contrast suffers. Therefore, if the SWNTs work as a contrast agent at lower rf frequencies, we can potentially achieve low-background, high-sensitivity, deep-tissue imaging.

The broad absorption range of SWNTs in the visible/NIR region[37] is also beneficial for optical imaging because one can use a wide range of laser wavelengths for imaging without the need to tune the contrast agent to a particular wavelength to optimize light absorption. In comparison, other contrast agents suitable for PAT, such as gold nanoparticles, are tuned to a particular wavelength range and can be used only with light within that range.[17,42] Furthermore, our results suggest that a minimum detectable concentration of SWNTs should be comparable to that of gold nanoparticles.[42] Using previously derived equations,[43] we have calculated that carbon nanotubes of 2 nm average diameter and 1 μm average length have $\sim 10^5$ carbon atoms, giving an average molecular weight of $\sim 10^6$ Da or g/mol (multiply the number of carbon atoms by

12, the atomic weight of carbon). From Fig. 3, it is clear that the minimum detectable concentration is <0.1 mg/mL or 100 nM (0.1 mg/mL/10^6 g/mol), 1 M SWNTs concentration, allowing their detection in the nM range. It is also evident that even at 0.1-mg/mL SWNTs concentration, there is a 35% increase in peak-to-peak TA signal compared to DI water and a 32% increase in peak-to-peak PA signal compared to blood. For targeted molecular imaging applications, an important consideration is not only the enhancement, but also the signal generated by the SWNTs themselves. In this study, we have detected signals with very high signal-to-noise ratio (SNR$>$100 in both TA and PA) at 1 mg/mL SWNT concentration, suggesting that the minimum detectable SWNT concentration could be as low as 0.01 mg/mL or $\sim$10 nM with this system, making them suitable for *in vivo* applications in various tissues. In general, the minimum detectable concentration of an exogenous contrast agent by PAT/TAT is dependent on many factors, such as incident light/microwave energy, ultrasound detector sensitivity, data acquisition electronics, etc. For our future *in vivo* studies, the concentration(s) of the SWNTs will depend on the specific application and the sensitivity of the imaging system.[36,44]

The SWNTs also have a number of additional benefits. (*i*) Other than TAT and PAT, SWNTs can also be used as a contrast agent for other imaging modalities, such as MRI, PET, NIR optical imaging, and nuclear imaging.[22–25] Therefore, in a true sense they can work as a multi-modal contrast agent. (*ii*) The external carbon sheath of the SWNTs can be directly functionalized for targeting and drug delivery. This capability is not possible for other optical contrast agents, such as gold nanoparticles, where one does not functionalize the gold, but rather the capping agents or the biocompatible coating used to stabilize and/or dispense gold nanoparticles in solution. (*iii*) SWNTs now offer the exciting and tantalizing prospect of achieving TAT and/or PAT molecular imaging and simultaneous therapy by NIR and rf-induced hyperthermia. Recently, SWNTs have been shown to facilitate the NIR and rf-induced ablation of tumor cells/tissues.[25,45] Thus, these unique features of SWNTs should allow the design of multimodal imaging and multitherapeutic approaches within a single platform.

4 Conclusions

In summary, we have successfully shown that SWNTs provide more than twofold signal enhancement in TAT at 3 GHz and more than sixfold signal enhancement in PAT at 1064 nm. These results indicate that by using SWNTs as contrast agents, the functional information from TAT and PAT together with other structural imaging modalities will be advantageous for early cancer diagnosis. At lower rfs, these exogenous contrast agents offer a new paradigm for low-background, high-sensitivity, deep-tissue, and targeted molecular imaging by TAT.

Acknowledgments

This work was sponsored by National Institutes of Health Grants No. R01 EB000712, No. R01 NS46214 (Bioengineering Research Partnerships), No. R01 EB008085, and No. U54 CA136398 (Network for Translational Research) (L.V.) and the Office of the Vice President of Research at Stony Brook University, Carol M. Baldwin fund (S.B.). L.W. has a financial interest in Endra, Inc., which, however, did not support this work. The authors thank Dr. Oleg Gang and Dr. Huming Xiong at the Center for Functional Nanomaterials, Brookhaven National Laboratory for access to the AFM, Tom Salagaj and Christopher Jensen at FirstNano/CVD Equipment Corporation for access to their CVD facilities, and Dr. Eunah Lee at Horiba JvonYvon, Edison, New Jersey, for the Raman spectroscopy measurements.

References

1. L. Ottobrini, P. Ciana, A. Biserni, G. Lucignani, and A. Maggi, "Molecular imaging: a new way to study molecular processes in vivo," *Mol. Cell Endocrinol.* **246**(1–2), 69–75 (2006).
2. V. Ntziachristos, J. Ripoll, L. H. V. Wang, and R. Weissleder, "Looking and listening to light: the evolution of whole-body photonic imaging," *Nat. Biotechnol.* **23**(3), 313–320 (2005).
3. S. R. Meikle, P. Kench, M. Kassiou, and R. B. Banati, "Small animal SPECT and its place in the matrix of molecular imaging technologies," *Phys. Med. Biol.* **50**(22), R45–R61 (2005).
4. J. V. Frangioni, "*In vivo* near-infrared fluorescence imaging," *Curr. Opin. Chem. Biol.* **7**(5), 626–634 (2003).
5. W. Krause, *Contrast Agents II: Optical, Ultrasound, X-Ray Imaging and Radiopharmaceutical Imaging*, Springer, New York (2002).
6. E. L. Ritman, "Molecular imaging in small animals—roles for micro-CT," *J. Cell. Biochem.* **39**, 116–124 (2002).
7. L. H. V. Wang, X. M. Zhao, H. T. Sun, and G. Ku, "Microwave-induced acoustic imaging of biological tissues," *Rev. Sci. Instrum.* **70**(9), 3744–3748 (1999).
8. G. Ku, B. D. Fornage, X. Jin, M. H. Xu, K. K. Hunt, and L. H. V. Wang, "Thermoacoustic and photoacoustic tomography of thick biological tissues toward breast imaging," *Technol. Cancer Res. Treat.* **4**(5), 559–565 (2005).
9. X. D. Wang, Y. J. Pang, G. Ku, X. Y. Xie, G. Stoica, and L. H. V. Wang, "Noninvasive laser-induced photoacoustic tomography for structural and functional *in vivo* imaging of the brain," *Nat. Biotechnol.* **21**(7), 803–806 (2003).
10. G. Ku, X. D. Wang, X. Y. Xie, G. Stoica, and L. H. V. Wang, "Imaging of tumor angiogenesis in rat brains in vivo by photoacoustic tomography," *Appl. Opt.* **44**(5), 770–775 (2005).
11. M. L. Li, J. T. Oh, X. Y. Xie, G. Ku, W. Wang, C. Li, G. Lungu, G. Stoica, and L. H. V. Wang, "Simultaneous molecular and hypoxia imaging of brain tumors *in vivo* using spectroscopic photoacoustic tomography," *Proc. IEEE* **96**(3), 481–489 (2008).
12. M. Pramanik, G. Ku, C. H. Li, and L. H. V. Wang, "Design and evaluation of a novel breast cancer detection system combining both thermoacoustic (TA) and photoacoustic (PA) tomography," *Med. Phys.* **35**(6), 2218–2223 (2008).
13. R. A. Kruger, K. D. Miller, H. E. Reynolds, W. L. Kiser, D. R. Reinecke, and G. A. Kruger, "Breast cancer *in vivo*: contrast enhancement with thermoacoustic CT at 434 MHz—Feasibility study," *Radiology* **216**(1), 279–283 (2000).
14. R. A. Kruger, D. R. Reinecke, and G. A. Kruger, "Thermoacoustic computed tomography-technical considerations," *Med. Phys.* **26**(9), 1832–1837 (1999).
15. A. A. Oraevsky, E. V. Savateeva, S. V. Solomatin, A. A. Karabutov, V. G. Andreev, Z. Gatalica, T. Khamapirad, and P. M. Henrichs, "Optoacoustic imaging of blood for visualization and diagnostics of breast cancer," in *Biomedical Optoacoustics III*, *Proc. SPIE* **4618**, 81–94 (2002).
16. M. H. Xu and L. H. V. Wang, "Photoacoustic imaging in biomedicine," *Rev. Sci. Instrum.* **77**(4), 041101 (2006).
17. Y. W. Wang, X. Y. Xie, X. D. Wang, G. Ku, K. L. Gill, D. P. O'Neal, G. Stoica, and L. H. V. Wang, "Photoacoustic tomography of a nanoshell contrast agent in the *in vivo* rat brain," *Nano Lett.* **4**(9), 1689–1692 (2004).
18. X. D. Wang, X. Y. Xie, G. N. Ku, and L. H. V. Wang, "Noninvasive imaging of hemoglobin concentration and oxygenation in the rat brain using high-resolution photoacoustic tomography," *J. Biomed. Opt.* **11**(2), 024015 (2006).
19. G. F. Lungu, M. L. Li, X. Y. Xie, L. H. V. Wang, and G. Stoica, "*In vivo* imaging and characterization of hypoxia-induced neovascularization and tumor invasion," *Int. J. Oncol.* **30**(1), 45–54 (2007).
20. B. P. Schneider and K. D. Miller, "Angiogenesis of breast cancer," *J.*

Clin. Oncol. **23**(8), 1782–1790 (2005).
21. P. Vaupel, A. Mayer, S. Briest, and M. Hockel, "Hypoxia in breast cancer: role of blood flow, oxygen diffusion distances, and anemia in the development of oxygen depletion," presented at *Oxygen Transport to Tissue XXVI*, Vol. **566**, pp. 333–342 (2005).
22. B. Sitharaman, K. R. Kissell, K. B. Hartman, L. A. Tran, A. Baikalov, I. Rusakova, Y. Sun, H. A. Khant, S. J. Ludtke, W. Chiu, S. Laus, E. Toth, L. Helm, A. E. Merbach, and L. J. Wilson, "Superparamagnetic gadonanotubes are high-performance MRI contrast agents," *Chem. Commun. (Cambridge)* **31**, 3915–3917 (2005).
23. M. R. McDevitt, D. Chattopadhyay, B. J. Kappel, J. S. Jaggi, S. R. Schiffman, C. Antczak, J. T. Njardarson, R. Brentjens, and D. A. Scheinberg, "Tumor targeting with antibody-functionalized, radiolabeled carbon nanotubes," *J. Nucl. Med.* **48**(7), 1180–1189 (2007).
24. Z. Liu, W. B. Cai, L. N. He, N. Nakayama, K. Chen, X. M. Sun, X. Y. Chen, and H. J. Dai, "*In vivo* biodistribution and highly efficient tumour targeting of carbon nanotubes in mice," *Nat. Nanotechnol.* **2**(1), 47–52 (2007).
25. P. Cherukuri, C. J. Gannon, T. K. Leeuw, H. K. Schmidt, R. E. Smalley, S. A. Curley, and R. B. Weisman, "Mammalian pharmacokinetics of carbon nanotubes using intrinsic near-infrared fluorescence," *Proc. Natl. Acad. Sci. U.S.A.* **103**(50), 18882–18886 (2006).
26. M. E. Hughes, E. Brandin, and J. A. Golovchenko, "Optical absorption of DNA-carbon nanotube structures," *Nano Lett.* **7**(5), 1191–1194 (2007).
27. S. Berciaud, L. Cognet, P. Poulin, R. B. Weisman, and B. Lounis, "Absorption spectroscopy of individual single-walled carbon nanotubes," *Nano Lett.* **7**(5), 1203–1207 (2007).
28. C. J. Gannon, P. Cherukuri, B. I. Yakobson, L. Cognet, J. S. Kanzius, C. Kittrell, R. B. Weisman, M. Pasquali, H. K. Schmidt, R. E. Smalley, and S. A. Curley, "Carbon nanotube-enhanced thermal destruction of cancer cells in a noninvasive radiofrequency field," *Cancer* **110**(12), 2654–2665 (2007).
29. IEEE standard for safety levels with respect to human exposure to radio frequency electromagnetic fields 3 kHz to 300 GHz, IEEE Std C95.1 (1999).
30. Laser Institute of America, American National Standard for Safe Use of Lasers ANSI Z136.1-2000, American National Standards Institute, Inc., New York (2000).
31. K. H. Song and L. H. V. Wang, "Deep reflection-mode photoacoustic imaging of biological tissue," *J. Biomed. Opt.* **12**(6), 060503 (2007).
32. Q. Fu, S. M. Huang, and J. Liu, "Chemical vapor depositions of single-walled carbon nanotubes catalyzed by uniform Fe2O3 nanoclusters synthesized using diblock copolymer micelles," *J. Phys. Chem. B* **108**(20), 6124–6129 (2004).
33. M. S. Dresselhaus, G. Dresselhaus, R. Saito, and A. Jorio, "Raman spectroscopy of carbon nanotubes," *Phys. Rep.* **409**(2), 47–99 (2005).
34. B. White, S. Banerjee, S. O'Brien, N. J. Turro, and I. P. Herman, "Zeta-potential measurements of surfactant-wrapped individual single-walled carbon nanotubes," *J. Phys. Chem. C* **111**(37), 13684–13690 (2007).
35. S. S. Chaudhary, R. K. Mishra, A. Swarup, and J. M. Thomas, "Dielectric-properties of normal and malignant human-breast tissues at radiowave and microwave-frequencies," *Indian J. Biochem. Biophys.* **21**(1), 76–79 (1984).
36. M. Pramanik, K. H. Song, M. Swierczewska, D. Green, B. Sitharaman, and L. H. V. Wang, "*In vivo* carbon nanotube-enhanced noninvasive photoacoustic mapping of the sentinel lymph node," *Phys. Med. Biol.* **54**(11), 3291–3301 (1984).
37. M. J. O'Connell, S. M. Bachilo, C. B. Huffman, V. C. Moore, M. S. Strano, E. H. Haroz, K. L. Rialon, P. J. Boul, W. H. Noon, C. Kittrell, J. P. Ma, R. H. Hauge, R. B. Weisman, and R. E. Smalley, "Band gap fluorescence from individual single-walled carbon nanotubes," *Science* **297**(5581), 593–596 (2002).
38. A. Saib, L. Bednarz, R. Daussin, C. Bailly, X. Lou, J. M. Thomassin, C. Pagnoulle, C. Detrembleur, R. Jerome, and I. Huynen, "Carbon nanotube composites for broadband microwave absorbing materials," *IEEE Trans. Microwave Theory Tech.* **54**(6), 2745–2754 (2006).
39. C. A. Grimes, C. Mungle, D. Kouzoudis, S. Fang, and P. C. Eklund, "The 500 MHz to 5.50 GHz complex permittivity spectra of single-wall carbon nanotube-loaded polymer composites," *Chem. Phys. Lett.* **319**(5–6), 460–464 (2000).
40. P. C. P. Watts, W. K. Hsu, A. Barnes, and B. Chambers, "High permittivity from defective multiwalled carbon nanotubes in the X-band," *Adv. Mater.* **15**(7–8), 600–603 (2003).
41. X. Jin, A. Keho, K. Meissner, and L. H. V. Wang, "Iron-oxide nanoparticles as a contrast agent in thermoacoustic tomography," *Proc. SPIE* **6437**, 64370E (2007).
42. M. Eghtedari, A. Oraevsky, J. A. Copland, N. A. Kotov, A. Conjusteau, and M. Motamedi, "High sensitivity of *in vivo* detection of gold nanorods using a laser optoacoustic imaging system," *Nano Lett.* **7**(7), 1914–1918 (2007).
43. K. Yamamoto, T. Kamimura, and K. Matsumoto, "Nitrogen doping of single-walled carbon nanotube by using mass-separated low-energy ion beams," *Jpn. J. Appl. Phys.* **44**(4A), 1611–1614 (2005).
44. A. De La Zerda, C. Zavaleta, S. Keren, S. Vaithilingam, S. Bodapati, Z. Liu, J. Levi, B. R. Smith, T. J. Ma, O. Oralkan, Z. Cheng, X. Y. Chen, H. J. Dai, B. T. Khuri-Yakub, and S. S. Gambhir, "Carbon nanotubes as photoacoustic molecular imaging agents in living mice," *Nat. Nanotechnol.* **3**(9), 557–562 (2008).
45. N. W. S. Kam, M. O'Connell, J. A. Wisdom, and H. J. Dai, "Carbon nanotubes as multifunctional biological transporters and near-infrared agents for selective cancer cell destruction," *Proc. Natl. Acad. Sci. U.S.A.* **102**(33), 11600–11605 (2005).